

RESEARCH ARTICLE SUMMARY

PHOTOENZYMES

Mechanism and dynamics of fatty acid photodecarboxylase

D. Sorigué, K. Hadjidemetriou, S. Blangy, G. Gotthard, A. Bonvalet, N. Coquelle, P. Samire, A. Aleksandrov, L. Antonucci, A. Benachir, S. Boutet, M. Byrdin, M. Cammarata, S. Carbajo, S. Cuiné, R. B. Doak, L. Foucar, A. Gorel, M. Grünbein, E. Hartmann, R. Hienerwadel, M. Hilpert, M. Kloos, T. J. Lane, B. Légeret, P. Legrand, Y. Li-Beisson, S. L. Y. Moulin, D. Nurizzo, G. Peltier, G. Schirò, R. L. Shoeman, M. Sliwa, X. Solinas, B. Zhuang, T. R. M. Barends, J.-P. Colletier, M. Joffre, A. Royant, C. Berthomieu*, M. Weik*, T. Domratcheva*, K. Brettel, M. H. Vos*, I. Schlichting*, P. Arnoux*, P. Müller*, F. Beisson*

INTRODUCTION: Photoenzymes are rare biocatalysts driven by absorption of a photon at each catalytic cycle; they inspire development of artificial photoenzymes with valuable activities. Fatty acid photodecarboxylase (FAP) is a natural photoenzyme that has potential applications in the bio-based production of hydrocarbons, yet its mechanism is far from fully understood.

RATIONALE: To elucidate the mechanism of FAP, we studied the wild-type (WT) enzyme from *Chlorella variabilis* (CvFAP) and variants with altered active-site residues using a wealth of techniques, including static and time-resolved crystallography and spectroscopy, as well as biochemical and computational approaches.

RESULTS: A 1.8-Å-resolution CvFAP x-ray crystal structure revealed a dense hydrogen-bonding network positioning the fatty acid carboxyl group in the vicinity of the flavin adenine dinucleotide (FAD) cofactor. Structures solved from free electron laser and low-dose synchrotron x-ray crystal data further highlighted an

unusual bent shape of the oxidized flavin chromophore, and showed that the bending angle (14°) did not change upon photon absorption (step 1) or throughout the photocycle. Calculations showed that bending substantially affected the energy levels of the flavin. Structural and spectroscopic analysis of WT and mutant proteins targeting two conserved active-site residues, R451 and C432, demonstrated that both residues were crucial for proper positioning of the substrate and water molecules and for oxidation of the fatty acid carboxylate by $^1\text{FAD}^*$ (~300 ps in WT FAP) to form $\text{FAD}^{\bullet-}$ (step 2). Time-resolved infrared spectroscopy demonstrated that decarboxylation occurred quasi-instantaneously upon this forward electron transfer, consistent with barrierless bond cleavage predicted by quantum chemistry calculations and with snapshots obtained by time-resolved crystallography. Transient absorption spectroscopy in H_2O and D_2O buffers indicated that back electron transfer from $\text{FAD}^{\bullet-}$ was coupled to and limited by transfer of an exchangeable proton or hydrogen atom

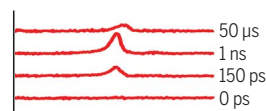
(step 3). Unexpectedly, concomitant with $\text{FAD}^{\bullet-}$ reoxidation (to a red-shifted form FAD_{RS}) in 100 ns, most of the CO_2 product was converted, most likely into bicarbonate (as inferred from FTIR spectra of the cryotrapped FAD_{RS} intermediate). Calculations indicated that this catalytic transformation involved an active-site water molecule. Cryo-Fourier transform infrared spectroscopy studies suggested that bicarbonate formation (step 4) was preceded by deprotonation of an arginine residue (step 3). At room temperature, the remaining CO_2 left the protein in 1.5 μs (step 4'). The observation of residual electron density close to C432 in electron density maps derived from time-resolved and cryocrystallography data suggests that this residue may play a role in stabilizing CO_2 and/or bicarbonate. Three routes for alkane formation were identified by quantum chemistry calculations; the one shown in the figure is favored by the ensemble of experimental data.

CONCLUSION: We provide a detailed and comprehensive characterization of light-driven hydrocarbon formation by FAP, which uses a remarkably complex mechanism including unique catalytic steps. We anticipate that our results will help to expand the green chemistry toolkit. ■

The list of author affiliations is available in the full article online.
*Corresponding author. Email: frederic.beisson@cea.fr (F.B.), pavel.muller@i2bc.paris-saclay.fr (P.M.), pascal.arnoux@cea.fr (P.A.), Ilme.schlichting@mpimf-heidelberg.mpg.de (I.S.), marten.vos@polytechnique.edu (M.H.V.), tatjana.domratcheva@mpimf-heidelberg.mpg.de (T.D.), martin.weik@ibs.fr (M.W.), catherine.berthomieu@cea.fr (C.B.)
Cite this article as D. Sorigué et al., *Science* 372, eabd5687 (2021). DOI: 10.1126/science.abd5687

READ THE FULL ARTICLE AT
<https://doi.org/10.1126/science.abd5687>

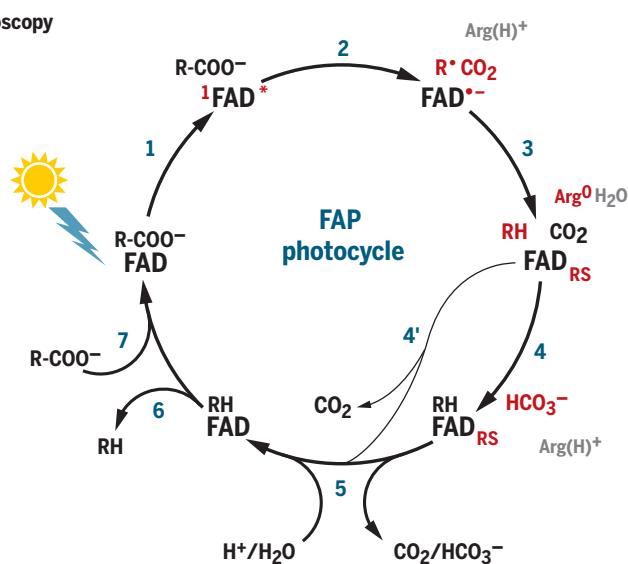
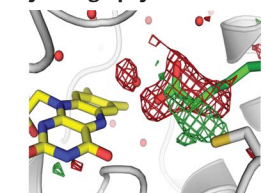
Multiscale time-resolved infrared spectroscopy



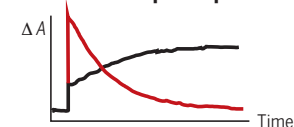
Fourier transform infrared spectroscopy



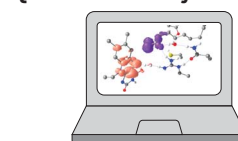
Time-resolved serial femtosecond crystallography



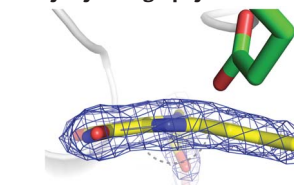
Transient absorption spectroscopy



Quantum chemistry



X-ray crystallography



Elucidation of the FAP photocycle by combining spectroscopic, biochemical, crystallographic, and computational studies.

RESEARCH ARTICLE

PHOTOENZYMES

Mechanism and dynamics of fatty acid photodecarboxylase

D. Sorigué¹, K. Hadjidemetriou², S. Blangy¹, G. Gotthard³, A. Bonvalet⁴, N. Coquelle⁵, P. Samire^{1,6}, A. Aleksandrov⁴, L. Antonucci⁴, A. Benachir⁴, S. Boutet⁷, M. Byrdin², M. Cammarata^{8,†}, S. Carbajo⁷, S. Cuiné¹, R. B. Doak⁹, L. Foucar⁹, A. Gorel⁹, M. Grünbein⁹, E. Hartmann⁹, R. Hienerwadel¹, M. Hilpert⁹, M. Kloos^{9,†}, T. J. Lane⁷, B. Légeret¹, P. Legrand¹⁰, Y. Li-Beisson¹, S. L. Y. Moulin¹, D. Nurizzo³, G. Peltier¹, G. Schirò², R. L. Shoeman⁹, M. Sliwa¹¹, X. Solinas⁴, B. Zhuang^{4,6}, T. R. M. Barends⁹, J.-P. Colletier², M. Joffre⁴, A. Royant^{2,3}, C. Berthomieu^{1*}, M. Weik^{2*}, T. Domratcheva^{9,12*}, K. Brettel⁶, M. H. Vos^{4*}, I. Schlichting^{9*}, P. Arnoux^{1*}, P. Müller^{6*}, F. Beisson^{1*}

Fatty acid photodecarboxylase (FAP) is a photoenzyme with potential green chemistry applications. By combining static, time-resolved, and cryotrapping spectroscopy and crystallography as well as computation, we characterized *Chlorella variabilis* FAP reaction intermediates on time scales from subpicoseconds to milliseconds. High-resolution crystal structures from synchrotron and free electron laser x-ray sources highlighted an unusual bent shape of the oxidized flavin chromophore. We demonstrate that decarboxylation occurs directly upon reduction of the excited flavin by the fatty acid substrate. Along with flavin reoxidation by the alkyl radical intermediate, a major fraction of the cleaved carbon dioxide unexpectedly transformed in 100 nanoseconds, most likely into bicarbonate. This reaction is orders of magnitude faster than in solution. Two strictly conserved residues, R451 and C432, are essential for substrate stabilization and functional charge transfer.

By far most enzymatic reactions in living cells are thermally activated, whereas reactions driven by light are much less common (1). Apart from photosynthetic reaction centers, three natural photoenzymes have been identified to date: DNA photolyases, which are involved in the repair of UV-damaged DNA (2); light-dependent prochlorophyllide oxidoreductase (LPOR), which is required for the maturation of chlorophyll (3); and the recently discovered fatty acid photodecarboxylase (FAP, EC 4.1.1.106), which converts fatty acids to hydrocarbons and CO₂ (4).

Photoenzymes require a photon for each turnover of a substrate molecule and offer the possibility to trigger and monitor catalytic steps and associated structural changes on very short time scales that are generally not accessible for thermally activated enzymes (5). Thus, over the past 20 years, the photochemical mechanism has been studied in detail for DNA photolyases (6–8) and has started to be identified for LPOR (9–13). Because of its readily available substrate, FAP may become a model of choice to understand catalytic steps that occur in enzymology.

Light-driven enzymes are also interesting for practical applications. Increasing our understanding and the repertoire of photoenzymatic mechanisms may help in the design of catalysts performing new reactions (14, 15) or in the development of new light-controlled proteins for optogenetics (16). FAP has potential biotechnological applications in green chemistry because hydrocarbons are important as cosmetics emollients, chemical synthons, solvents, and fuels (17–19). FAP complements routes previously identified for bio-based synthesis of hydrocarbons (20) by providing a one-step light-driven pathway from fatty acids. Rational design approaches have recently allowed improvement of the efficiency of FAP on high-value functionalized carboxylic acids (21) and on short-chain fatty acids to produce liquefied petroleum gas (20). Understanding the reaction mechanism of FAP in detail is thus of utmost importance, both from a fundamental research and an application point of view.

FAP is an algae-specific enzyme from the glucose-methanol-choline (GMC) oxidoreductase family harboring a flavin adenine dinucleotide (FAD) cofactor. It allows the decarboxylation

of C16–C18 free (nonesterified) fatty acids to the corresponding *n*-alka(ene)s (4). These hydrocarbon products are mostly located in chloroplast thylakoids, but their exact role is still unknown (22, 23). The initial spectroscopic characterization of FAP, which was based on monitoring the electronic state of the flavin after excitation by a laser flash, led to the first model of the FAP photocycle (4). The cycle starts with the quenching of the singlet excited state by forward electron transfer (fET) from bound fatty acid R-CO₂[−] in ~300 ps (with a quantum yield >80%), forming a flavin anion radical FAD^{•−} and a fatty acid radical R-CO₂[•]. The latter decarboxylates, yielding an alkyl radical R[•] and CO₂. FAD^{•−} is reoxidized in ~100 ns by back electron transfer (bET), which ultimately provides the electron for the reduction of R[•] to the alkane RH. FAD^{•−} reoxidation results in a transiently red-shifted flavin state FAD_{RS} that reverts to the initial state in 4 ms.

Despite this insight, several open questions remained, including: Which structural features of the FAP active site promote substrate stabilization and favor the fET? Is decarboxylation instantaneous upon this fET step or is it slowed by an activation barrier? Does conversion of R[•] to the alkane RH occur by bET from FAD^{•−} coupled to a proton transfer (PT/PCET) or by hydrogen atom transfer (HAT) from a nearby amino acid (4, 24)? What is the origin of the proton or the hydrogen atom? Here, we report a high-resolution structure of FAP and characterize key steps along the FAP photocycle using a wealth of static and time-resolved crystallographic and spectroscopic techniques, as well as computational approaches. Our detailed characterization of FAP reveals unforeseen mechanistic complexity.

High-resolution structure of CvFAP

Crystals of FAP from *C. variabilis* NC64A (CvFAP), diffracting x-rays to high resolution and without the twinning fault reported earlier (4), were obtained upon removal of the N-terminal helix involved in crystal packing (residues 61 to 76) in native CvFAP. The resulting structure, solved at 1.8-Å resolution (table S1), now provides a detailed view of the active-site architecture (Fig. 1, A to D, and fig. S1). Although no substrate was added during protein purification and crystallization, two C18 fatty acids copurified with FAP were clearly identified, one in the active site and the other

¹Aix-Marseille University, CEA, CNRS, Institute of Biosciences and Biotechnologies, BIAM Cadarache, 13108 Saint-Paul-lez-Durance, France. ²Université Grenoble Alpes, CEA, CNRS, Institut de Biologie Structurale, 38000 Grenoble, France. ³European Synchrotron Radiation Facility, 38043 Grenoble, France. ⁴LOB, CNRS, INSERM, Ecole Polytechnique, Institut Polytechnique de Paris, 91128 Palaiseau, France. ⁵Large-Scale Structures Group, Institut Laue Langevin, 38042 Grenoble Cedex 9, France. ⁶Université Paris-Saclay, CEA, CNRS, Institute for Integrative Biology of the Cell (I2BC), 91198 Gif-sur-Yvette, France. ⁷Linac Coherent Light Source (LCLS), SLAC National Accelerator Laboratory, Menlo Park, CA 94025, USA. ⁸Department of Physics, UMR URI-CNRS 6251, University of Rennes 1, F-Rennes, France. ⁹Max-Planck-Institut für medizinische Forschung, Jahnstrasse 29, 69120 Heidelberg, Germany. ¹⁰Synchrotron SOLEIL, L'Orme des Merisiers Saint-Aubin, BP 48, 91192 Gif-sur-Yvette, France. ¹¹Univ. Lille, CNRS, UMR 8516, LASIRE, Laboratoire de Spectroscopie pour les Interactions, la Réactivité et l'Environnement, 59000 Lille, France. ¹²Department of Chemistry, Lomonosov Moscow State University, Moscow 119991, Russia.

†Present address: European Synchrotron Radiation Facility (ESRF), F-38043 Grenoble, France. ‡Present address: Sample Environment and Characterization European XFEL, 22869 Schenefeld, Germany.

*Corresponding author. Email: frederic.beisson@cea.fr (F.B.); pavel.muller@i2bc.paris-saclay.fr (P.M.); pascal.arnoux@cea.fr (P.A.); ilme.schlichting@mpimf-heidelberg.mpg.de (I.S.); marten.vos@polytechnique.edu (M.H.V.); tatjana.domratcheva@mpimf-heidelberg.mpg.de (T.D.); martin.weik@ibs.fr (M.W.); catherine.berthomieu@cea.fr (C.B.)

on the surface of the protein. The latter is stabilized by hydrophobic interactions with nonpolar side chains (L427, Y419, I126, I416, and L420), as well as the aliphatic parts of R132 and R122. In the active site, the carboxyl group of the fatty acid is stabilized by hydrogen bonds with water molecules (Wat1 and Wat2) and the side chains of R451 and N575 (Fig. 1D). The fatty acid substrate is also stabilized on the dimethylbenzene side of FAD, in contrast to other GMC oxidoreductase enzymes, which have their substrate stabilized near the N5 atom of FAD (fig. S2).

Conformation of oxidized FAD in CvFAP

In the high-resolution dark-state structure of FAP obtained from synchrotron data “100 K dark,” the isoalloxazine ring of the FAD cofactor was found to be bent, with the dihedral angle C4-N5-N10-C9 (butterfly bending angle) deviating by 17.4° from planarity (Fig. 1E and fig. S2A). Such bending is usually interpreted as being caused by x-ray photoreduction con-

verting supposedly planar oxidized flavin to the bent reduced form (8, 25, 26). For FAP, however, in crystallo ultraviolet-visible (UV-Vis) absorption microspectrophotometry (fig. S3), low-dose crystallography, (fig. S4A and table S1), Raman microspectrophotometry (fig. S4, B and C), and molecular dynamics simulations (fig. S5, A and B) using a recent flavin force field (27) indicated that the FAD cofactor is bent in its oxidized form (supplementary text S1). To obtain a definite answer concerning the conformation of the oxidized FAD in FAP, we performed room temperature (RT) serial femtosecond crystallography (SFX) at an x-ray free-electron laser (XFEL; see below for details), which allows collecting essentially radiation damage-free diffraction data (28, 29). This SFX dark-state structure of FAP (“SFX dark”), solved at 2.0-Å resolution (table S2), features a FAD with a similar bending angle (14.3°) as observed in the synchrotron 100 K dark and the “RT dark low-dose” structures (Fig. 1E and figs. S4, S6, and S7), supporting

the notion that in FAP, the FAD cofactor is in a bent conformation in the oxidized state. To our knowledge, a butterfly bent conformation of the oxidized flavin has not been firmly established for any other flavoprotein. In fact, bent conformations were either not discussed in the literature or were attributed to x-ray-induced flavin reduction. Future radiation-damage-free structures of oxidized flavoproteins should reveal whether the bending is a feature specific to FAP.

New insights into the CvFAP photocycle by time-resolved spectroscopy

Our previous single-shot fluorescence and transient absorption experiments in the presence of substrate, with 100 ps and 10 ns temporal resolution, respectively, showed a decay of the singlet excited flavin ($^1\text{FAD}^*$) in ~300 ps and formation of $\text{FAD}^{\bullet-}$ within 10 ns (4). Here, we extended the fluorescence and visible absorption experiments to the ultrafast time scale with 100-fs-resolution pump-probe spectroscopy (Fig. 2, A and B, and fig. S8A), showing that no faster $^1\text{FAD}^*$ decay phases occurred [only an ~2-ps thermal relaxation phase was observed in the fluorescence as in other flavoproteins (30)] and that, as predicted (4), $\text{FAD}^{\bullet-}$ is formed concomitantly with $^1\text{FAD}^*$ decay (fig. S8B).

We investigated whether the carboxylate of the fatty acid is cleaved off concomitantly with electron transfer from the fatty acid to $^1\text{FAD}^*$ (~300 ps), after this oxidation, or accompanying the bET from flavin (~100 ns). Light-induced Fourier transform infrared (FTIR) difference spectroscopy performed at 298 K showed a CO_2 band at 2342 cm^{-1} (Fig. 2C), corresponding to CO_2 in solution (31). The kinetics of CO_2 formation in FAP were monitored by picosecond to microsecond time-resolved infrared spectroscopy (TR-IR) in a frequency range centered around 2350 cm^{-1} and arbitrary detuning asynchronous optical sampling (ADASOPS) (32, 33). This experiment showed the appearance of a CO_2 absorption band centered at 2337.5 cm^{-1} with a time constant of ~270 ps (Fig. 2, C to E, and fig. S9). We conclude that decarboxylation is rate-limited by electron transfer from substrate to $^1\text{FAD}^*$, occurring in ~300 ps. The initial CO_2 band frequency is ~5 cm^{-1} down-shifted with respect to that of $^{12}\text{CO}_2$ in aqueous solution, a finding that we assign to the protein environment. Subsequently, the CO_2 signal diminishes about fourfold with a time constant of 100 ns without changing much in shape, followed by an upshift toward 2342 cm^{-1} , a process fitted with a time constant of ~1.5 μs . The latter process likely reflects migration of CO_2 toward the solvent. The data indicate that the 100-ns process implies transformation of ~75% of the initially formed CO_2 within the protein into another molecule, possibly bicarbonate, concomitant with flavin reoxidation to the red-shifted form FAD_{RS} (see next

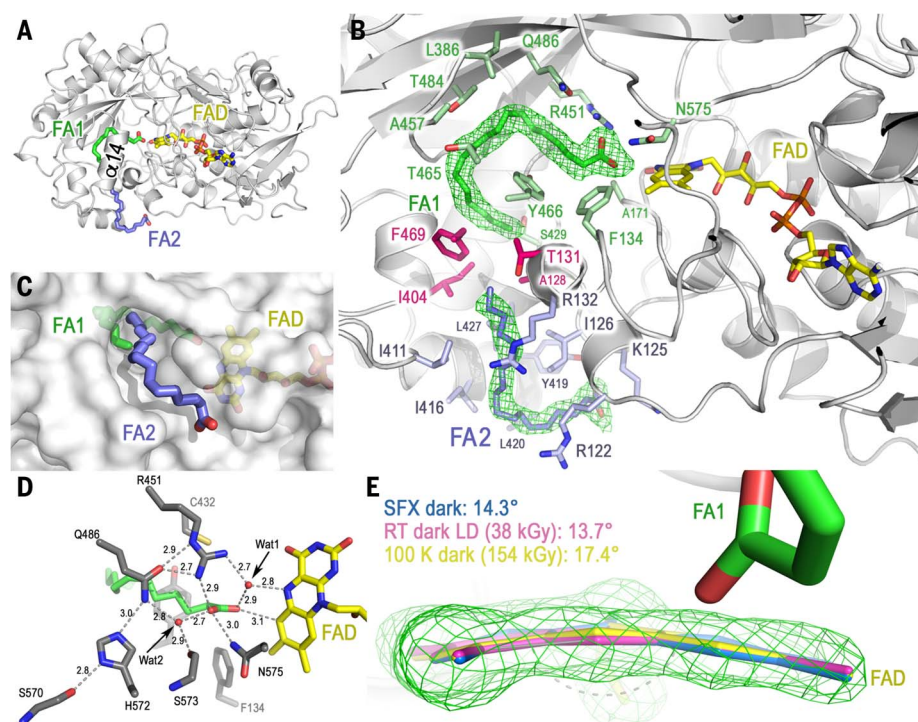


Fig. 1. High-resolution crystal structures of CvFAP. (A) Structure of CvFAP determined from synchrotron data at 100 K (100 K dark), including the FAD cofactor and two C18 fatty acid substrates (FA1 and FA2). (B) Binding of the two substrate molecules. The “omit” electron density map (5.0 σ contour level) is shown as a green mesh, and amino acid side chains in a radius of 4 Å around the binding site are shown as sticks (green: active site, blue: secondary binding site, purple: between sites). (C) Position of the peripheral substrate (FA2) partly obstructing the channel leading to the active site tunnel. (D) Close-up view of the catalytic site showing the water molecules Wat1 and Wat2 and the interactions with FAD (yellow sticks) and the substrate in the active site FA1 (green sticks). Distances are indicated in angstroms. The shortest distance between the substrate and the FAD cofactor (carboxylate O1-isoalloxazine C6) is 3.1 Å. The tail of the peripheral substrate points toward the entrance of a tunnel leading to the active site that is lined by A128, T131, I404, and F469. (E) Superposition of the FAD isoalloxazine rings from the SFX dark structure (blue; molecule A) and the synchrotron structures (pink: RT dark low-dose; yellow: 100 K dark). The SFX $F_{\text{obs}} - F_{\text{calc}}$ omit map at 3 σ (green) is overlaid, and the FAD bending angles are indicated.

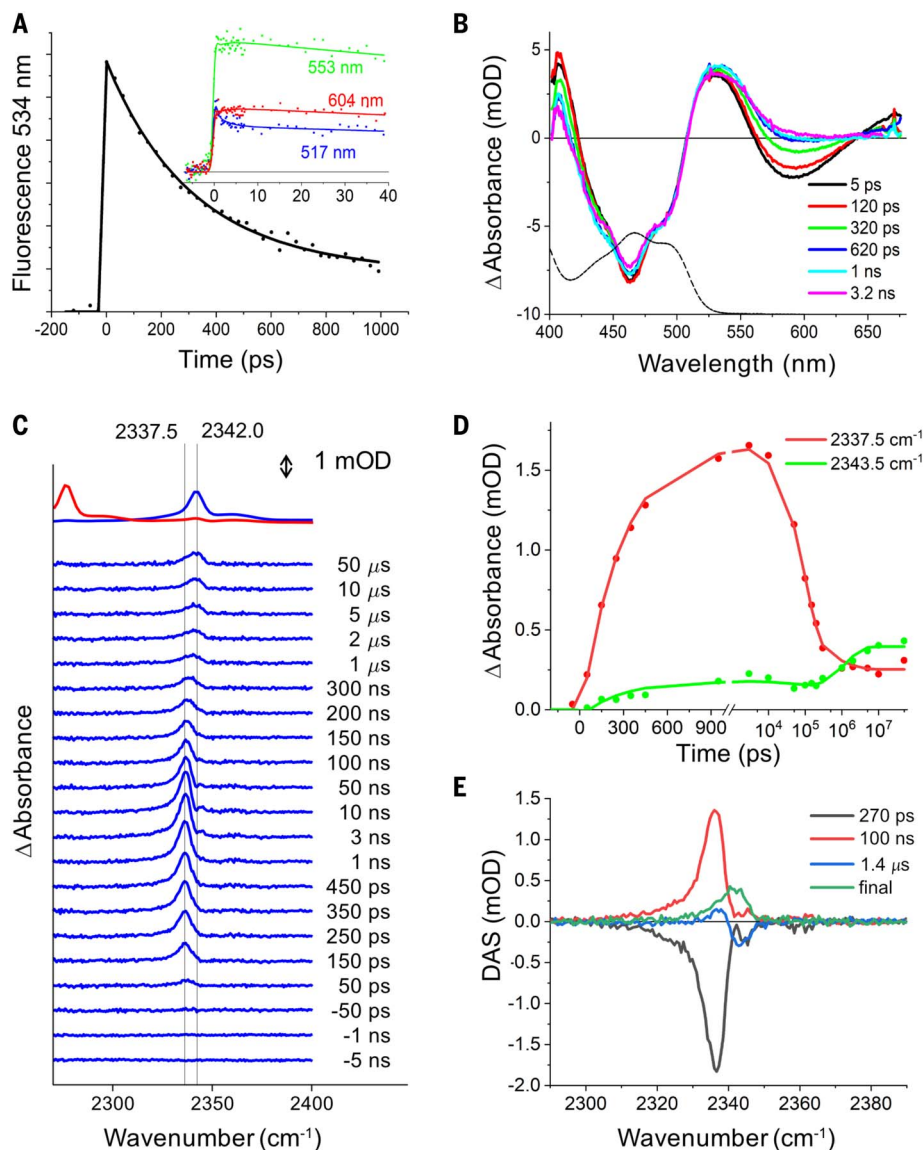


Fig. 2. Time-resolved infrared and UV-Vis spectroscopies of CvFAP. (A) Fluorescence kinetics reflecting $^1\text{FAD}^*$ decay. The solid line is a fit with time constants of 300 ps (85%) and 5 ns [the latter time constant was imposed according to (4)]. The inset shows an additional ~ 2 ps wavelength-dependent phase reflecting red shifting of the fluorescence spectrum caused by excited-state relaxation. (B) Transient visible absorption spectra at different delay times in the same time domain. The negative absorption features reflect bleaching of the FAD_{ox} resting state (<525 nm, the black dashed line is the ground state absorption spectrum) and stimulated emission (550 to 650 nm). Full transient fluorescence spectra and global analysis of the transient absorption spectra are shown in fig. S8. (C) Transient infrared spectra in the CO_2 spectral region on the picosecond-microsecond time scale. The vertical lines are guides for the eye and correspond to the maximum of released CO_2 in the protein and to the known maximum for CO_2 in aqueous solution, 2342 cm^{-1} (31). The upper traces correspond to independent steady-state 298 K light-induced FTIR difference spectra with ^{12}C -palmitate and ^{13}C -palmitate substrates (blue trace and red trace, respectively). (D) Kinetics at frequencies close to the initial and final maxima of released CO_2 . The lines are the result of a global fit. The time scale is linear up to 1 ns and logarithmic thereafter. (E) Decay-associated spectra (DAS) corresponding to a global fit of the data with three exponential phases (time constants of the fit are indicated) and a constant phase.

section on the red-shifted intermediate). This process was not foreseen in our previously proposed reaction scheme (4). Whereas our present data covering six orders of magnitude in time can be reasonably well described with

these three exponential processes and a constant phase (Fig. 2E), it is possible that an additional phase of CO_2 release into the solvent occurs on a time scale exceeding $50\text{ }\mu\text{s}$, the temporal window of our present experiments.

To determine whether any of the reaction steps are coupled to or directly reflect PT or HAT, we compared the kinetics of all steps observable by continuous-probe time-resolved fluorescence or transient absorption spectroscopy in H_2O and D_2O buffers. The biphasic fluorescence signal showing the decay of $^1\text{FAD}^*$ [caused by quenching by ET from the substrate (300 ps phase; $>80\%$) and by the intersystem-crossing to a nonreactive triplet state (~ 6.5 ns phase; $<20\%$)] was not visibly affected by the isotope exchange (Fig. 3A), as expected for reactions that are not substantially coupled to movements of exchangeable hydrogen species [e.g., back-ET from Q_A^- to P680^+ in photosystem II (34)]. By contrast, the kinetics of $\text{FAD}^{\bullet-}$ reoxidation to FAD_{RS} observed by transient absorption spectroscopy at three characteristic wavelengths slowed down by a factor of ~ 2 , from ~ 100 ns in H_2O to ~ 200 ns in D_2O (Fig. 3B), suggesting that this bET step is coupled to and limited by transfer of an exchangeable proton or hydrogen atom. Change of buffer pH in the interval between 7.5 and 9.1 had no effect on the kinetics of this step (fig. S10A), indicating that the proton or hydrogen atom donor involved in the reaction has a pK_a value >9.1 (where K_a is the acid dissociation constant). The significantly lower kinetic isotope effect (KIE) of 1.2 reported by Heyes *et al.* (24) might be due to insufficient time-resolution of their experiment (see supplementary text S4).

The last step observable by transient absorption spectroscopy was the disappearance of the transient red shift of reoxidized FAD occurring in a few milliseconds. This process was previously (4) assigned to reprotonation of X^- , the conjugate base of XH , an unidentified proton donor to the alkyl radical. Kinetics of this process also slowed down from ~ 3 to ~ 10 ms when H_2O in the buffer was replaced by D_2O (Fig. 3C). Consistent with this observation and the recent report of a pH increase (in an unbuffered solution) associated with this step (24), this process apparently reflects a proton transfer from bulk solvent. Again, change of buffer pH in the interval between 7.5 and 9.1 had no effect on the kinetics of this step (fig. S10B), nor did the consumption of the native substrate (fig. S10C). Time-resolved spectroscopic findings are summarized in fig. S11.

Photodecarboxylation and characterization of the red-shifted intermediate at cryogenic temperatures

Our time-resolved spectroscopic results predicted that a fraction of the CO_2 product is present in the active site in the red-shifted photoproduct intermediate. For a detailed characterization by static methods, we tried to stabilize this intermediate using cryotrapping. UV-Vis absorption spectra of CvFAP crystals

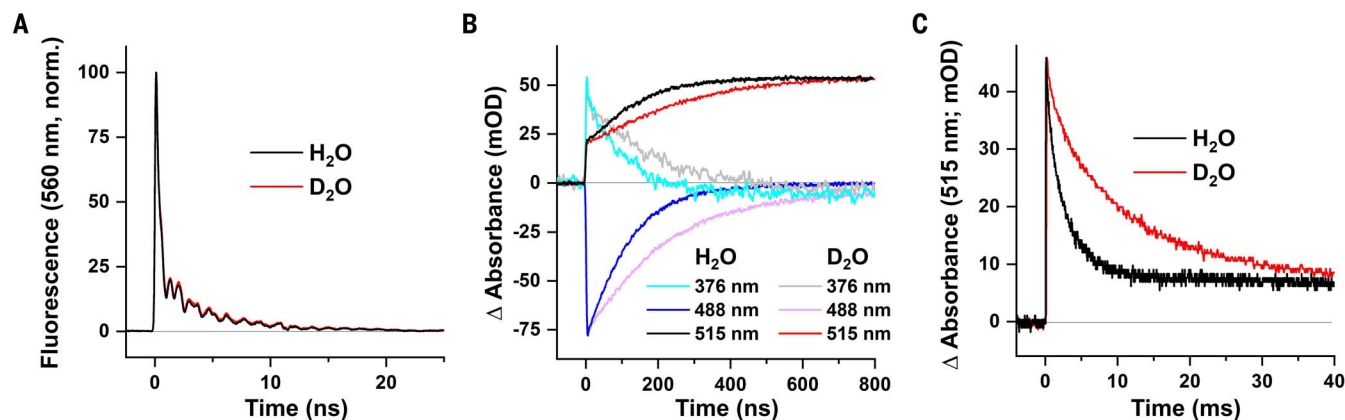


Fig. 3. Effects of H₂O-D₂O exchange on time-resolved fluorescence and UV-Vis spectroscopy of CvFAP. (A) Normalized signals of time-resolved fluorescence of ¹FAD* at 560 nm in H₂O and D₂O buffers. (B) Effect of H₂O-to-D₂O exchange on the kinetics of FAD^{•-} reoxidation to FAD_{RS}, followed by transient absorption spectroscopy at selected wavelengths on a submicrosecond time scale. (C) Effect of H₂O to D₂O buffer exchange on the decay of FAD_{RS} measured at 515 nm on the millisecond time scale.

and solutions exposed to increasing amounts of blue light at 100 K indeed revealed the gradual conversion into a red-shifted form similar to that previously observed at RT [(4) and fig. S12]. These conditions were used to further characterize the red-shifted intermediate using light-induced FTIR difference spectroscopy. To identify IR modes of the substrate and products of the reaction, we replaced the native substrate with 1-¹²C or 1-¹³C palmitate. The identification of characteristic ¹³C-sensitive IR bands of carboxylate in the FTIR difference spectra at 1541 and 1391 cm⁻¹ shows that the substrate initially was in the deprotonated form (Fig. 4A, i and ii; details supporting all IR bands assignments mentioned below are given in supplementary text S2). A peak at 2340 cm⁻¹ (Fig. 4A, v) was assigned to formation of CO₂ from 1-¹²C-palmitate and at 2274 cm⁻¹ from 1-¹³C-palmitate. When comparing FTIR spectra recorded with FAP samples containing 1-¹²C- and 1-¹³C-palmitate, small bands were also observed at 1356 to 1335 cm⁻¹ and 1312 cm⁻¹ (Fig. 4A, iii), which is indicative of the formation of trace amounts of ¹²C and ¹³C bicarbonate, respectively. We repeated the FTIR experiments at 150 K. At this temperature, the CO₂ band was small (Fig. 4A, v), whereas large positive bands at 1646 (1614) and 1352 (1318) cm⁻¹ were detected that could be unambiguously assigned to IR modes of ¹²C- (¹³C-) bicarbonate (Fig. 4A, iv). The FTIR data thus demonstrate the buildup of bicarbonate at 150 K and indicate that its formation at 100 K is limited by an energy barrier.

The structure derived from a CvFAP crystal exposed to 470 nm light at 100 K ("100 K light") featured FAP trapped in a FAD_{RS} state, as shown by in crystallo microspectrophotometry (fig. S12). The difference electron density map between 100 K light and 100 K dark displays strong and significant peaks only

around the substrate and FAD cofactor. These peaks can be fitted with a CO₂ molecule in addition to the alkyl chain stabilized in the active site (Fig. 4, B and C, and fig. S13, A to C). The positive difference electron density along the aliphatic tail of the substrate (from C13 to C15) and the 8° rotation of the side chain of Y466 indicates a correlated motion consistent with the strong electronic coupling observed by quantum chemistry between the substrate and Y466. To reflect the optimum pH of FAP in solution [pH 8.5 (4)] and to overcome thermal activation barriers, a FAP crystal was soaked at pH 8.5 and illuminated at 150 K ("150 K light"). After modeling alkane and a CO₂ molecule, the residual $F_o - F_c$ electron density map showed a positive density with a triangular shape close to C432, which we tentatively attributed to bicarbonate with 30% occupancy (Fig. 4D and fig. S14).

Time-resolved serial femtosecond crystallography of CvFAP

We investigated the structural changes occurring in FAP after photoexcitation at RT by a time-resolved SFX (TR-SFX) experiment (35) using a pump-probe scheme. Time-resolved fluorescence spectroscopy on FAP microcrystals established that the kinetics of fFET are the same as in solution (supplementary text S5 and fig. S15). For TR-SFX at the Linac Coherent Light Source (LCLS), FAP microcrystals were photoexcited by picosecond 400-nm pump pulses and probed by femtosecond XFEL pulses after pump-probe delays of 20 ps, 900 ps, 300 ns, and 2 μs to cover time scales on which FAD reduction and FAD^{•-} reoxidation occur. The SFX dark state structure mentioned above was determined from the data in the absence of a pump laser pulse. Structural changes after photoexcitation were visualized as positive and negative peaks in difference Fourier electron density maps calculated between the

light and dark datasets ($F_{\text{obs}}^{\text{light}, \Delta t} - F_{\text{obs}}^{\text{dark}}$, Fig. 5A) at 2.2-Å resolution. The most prominent difference electron density peaks at all four time points were at the active site, with the highest negative peak (-5.5 to -10.1 σ, depending on the time point) at the position of the carboxyl group of the substrate, showing that light-induced decarboxylation occurred (Fig. 5A). At 900 ps, decarboxylation had occurred to a considerable extent, consistent with the 270-ps time constant determined by multiscale time-resolved IR spectroscopy (Fig. 2, C to E). At 300 ns and 2 μs, a strong negative peak was observed at Wat1 (-5.8, and -6.2 σ, respectively; Fig. 5A), but not on Wat2. We note the absence of positive difference electron density peaks associated with the photo-dissociated CO₂ in the vicinity of the substrate carboxyl group. A possible reason could be the small initial displacement of cleaved CO₂ relative to its position in the fatty acid, consistent with the structure determined based on an illuminated cryocooled crystal 100 K light (see fig. S13C for comparison). It is conceivable that the positive difference densities close to C432 in the 300-ns and 2-μs datasets (Fig. 5A) correspond to the feature(s) observed in the data obtained from cryocooled crystals illuminated at 150 K (Figs. 5B and 4D), tentatively assigned to a bicarbonate (fig. S14). In the SFX data, attempts to fit unambiguously this positive difference density with a bicarbonate, a CO₂ molecule, or a mixture thereof remained unsatisfactory. The absence of significant difference electron density peaks at the FAD at all four time points suggests that the isalloxazine ring does not undergo significant light-induced conformational changes.

Quantum chemistry study of CvFAP

We performed quantum chemistry calculations for the decarboxylation reaction in the active site of FAP, considering electronic

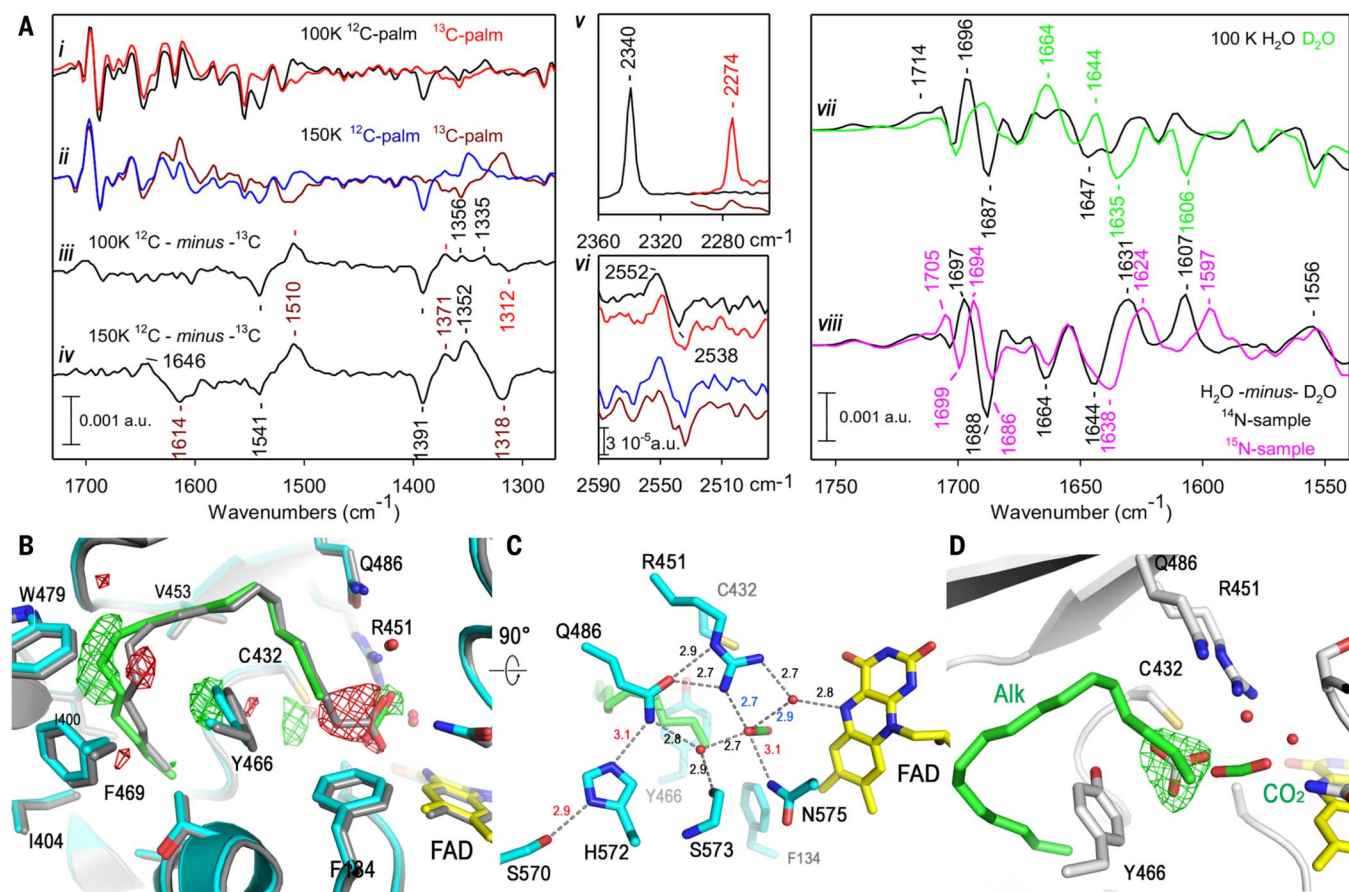


Fig. 4. Characterization of the CvFAP red-shifted intermediate at cryogenic temperatures. (A) Light-induced FTIR difference spectra recorded from FAP solutions (i) and (ii) and corresponding ^{12}C - minus ^{13}C difference spectra (iii) and (iv). The 2360 to 2260 cm^{-1} and 2590 to 2490 cm^{-1} regions of the spectra in (i) and (ii) are shown in (v) and (vi). For the spectrum in black, the FTIR spectrometer was continuously purged with N_2 to avoid contamination by gaseous CO_2 that might originate from a dry air purge. This was not the case for spectra recorded from FAP samples with $1\text{-}^{13}\text{C}$ -palmitate; these were cut off above 2300 cm^{-1} to avoid bands from gaseous CO_2 . (vii) Overlay of the spectra recorded at 100 K from FAP with ^{12}C -palmitate in H_2O (black) and in D_2O (green). (viii) $\text{H}_2\text{O} - \text{D}_2\text{O}$ difference spectra calculated for ^{14}N - and ^{15}N -labeled FAP samples. (B) Experimental difference

density map ($F_{\text{light}} - F_{\text{dark}}$, 100 K data) contoured at $\pm 4\sigma$ around the active-site substrate superimposed on the refined structures of the dark state (gray) and the red-shifted form (cyan, with FAD in yellow and alkane and CO_2 in green). The cleavage of the C1–C2 bond is clearly visible. (C) Details of the active site of FAP_{RS} formed upon illumination (UV-Vis spectra in fig. S12). All distances shorter than 3.2 Å are labeled, except the fatty acid O1–FAD C6 distance, which increases from 3.1 Å in the dark to 3.6 Å upon illumination (in CO_2). (D) $F_0 - F_c$ electron density omit map (3.5 σ) derived from crystals kept at 150 K and pH 8.5, showing positive difference electron density next to C432, consistent with a bicarbonate. Its potential interactions with the environment are shown in fig. S14. Uncleaved fatty acid (~30% occupancy) is omitted for clarity.

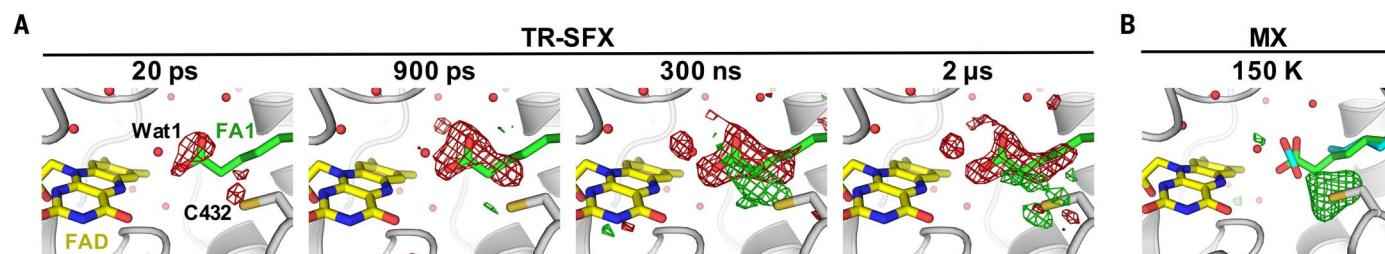


Fig. 5. Time-dependent changes in the CvFAP active site followed by TR-SFX. (A) Locally averaged q-weighted difference Fourier maps calculated between the SFX light and dark datasets ($F_{\text{obs}}^{\text{light}, \Delta t} - F_{\text{obs}}^{\text{dark}}$, with $\Delta t = 20$ ps, 900 ps, 300 ns, 2 μs). The 2.2-Å resolution maps are shown at $+4\sigma$ (green) and -4σ (red). The SFX dark-state model of molecule B is overlaid, with FAD in yellow, fatty acid in green, and the protein in gray. The q-weighted difference

maps for molecules A and B, i.e., without local averaging, are shown in fig. S31. (B) $F_{\text{obs}} - F_{\text{calc}}$ electron density (contoured at 3.5 σ) of Fig. 3E, shown in a different orientation, which features unmodeled positive electron density next to C432 that is reminiscent of a bicarbonate (Fig. 4D and fig. S14, see text), in a location similar to where positive difference density is present in the time-resolved maps at 300 ns and 2 μs .

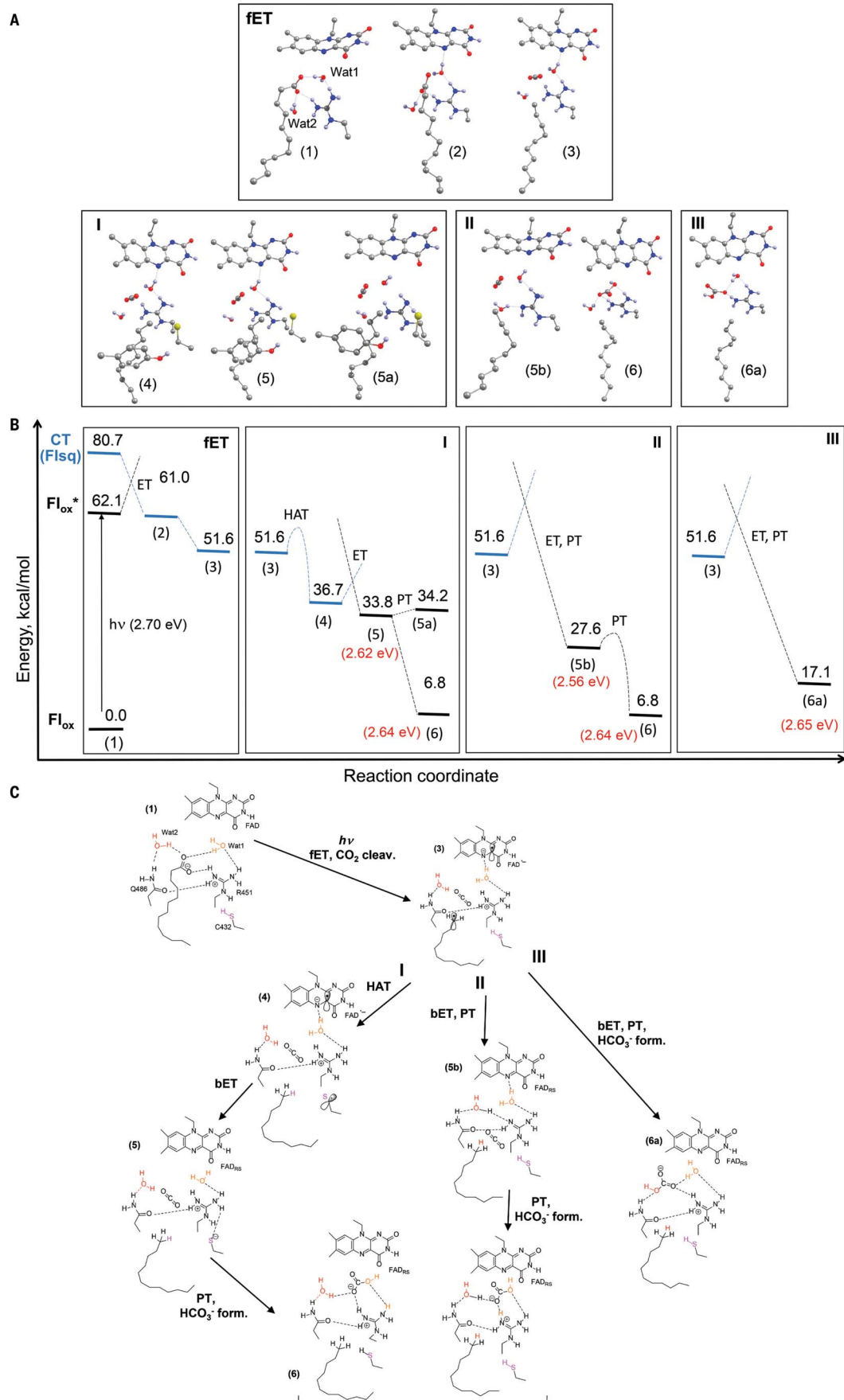


Fig. 6. Plausible CvFAP photoreaction pathways according to quantum chemistry calculations. (A) Structural changes accompanying decarboxylation and alkane formation in the FAP active site. Flavin butterfly-bending angle is 15° and 19° in the oxidized and semiquinone states, respectively. For clarity, only a small part of the active-site model is shown. The complete model is presented in fig. S16. (B) Energies of the reactants, intermediates, and products indicated in (A). Common to all pathways is fET mediated by Wat1 rearrangement (1) → (2) followed by CO₂ cleavage (2) → (3). Alkane formation occurs either

through HAT (pathway I) or PCET (pathways II and III). Pathway I consist of alkane formation through HAT from C432 (3) → (4), flavin reoxidation by the C432 radical (4) → (5), and C432 reprotonation and bicarbonate formation (5) → (6). Pathway II involves alkane formation through bET coupled to PT from Wat2 and subsequent R451 deprotonation (3) → (5b). Bicarbonate formation from CO₂ and Wat1 recovers protonated R451 (5b) → (6). In pathway III, bET is coupled to Wat2 deprotonation and formation of bicarbonate (3) → (6a). (C) Chemical scheme detailing intermediate states of fET and pathways I to III.

states relevant for flavin photoexcitation, electron transfer, decarboxylation, and alkane formation, as well as the effects of flavin bending (see supplementary text S6). To perform the reaction pathway calculations, a large active-site model (consisting of 272 atoms; fig. S16) was prepared using the coordinates of the high-resolution crystal structure of the dark state (Fig. 1D). Unexpectedly, computations indicated multiple routes to form an alkane in the FAP active site, as summarized in Fig. 6.

Common to all routes, photoexcitation triggered charge transfer (CT) from the substrate to the flavin. Interactions with two water molecules stabilized the anionic carboxylate substrate (1) (Fig. 6A). Removing these water molecules from the active site or rearranging Wat1 to form a hydrogen bond with flavin substantially decreased the energy of the CT state, i.e., of the flavin radical anion and the fatty acid radical (table S6). After Wat1 rearrangement, the CT energy was 15 kcal/mol lower than the excited-flavin energy (table S6). Concomitantly, electronic coupling between the flavin and substrate increased almost threefold, reaching 47 meV (table S7), thus favoring the transfer of an electron from the carboxylate. The formed carboxylic radical underwent a barrierless decarboxylation (fig. S17), affording the alkyl radical (3). The energy of the alkyl radical intermediate was 52 kcal/mol above the dark state (1), which corresponds to >80% of the photon energy (Fig. 6B). CO₂ dissociation increased the distance separation in the radical pair, and, accordingly, the electronic coupling between the alkyl and flavin radicals was only 7 meV (table S7).

From the alkyl radical (3), the alkane product (6/6a) can be formed through several reaction pathways (Fig. 6, pathways I to III). The chemical changes characterizing pathways I to III are summarized in Fig. 6C. HAT from a nearby residue has been discussed previously (4, 24). Our results indicate strong interactions with the Y466 phenolic side chain (electronic coupling 142 meV; table S7) that may facilitate migration of the alkyl radical toward Y466 and C432. The HAT reaction from C432 (Fig. 6, pathway I) proceeded through an energy barrier (9 kcal/mol; fig. S18) and led to a Cys-radical state (4) with a 15 kcal/mol lower energy than that of the alkyl radical intermediate (3). Re-oxidation of the flavin by C432 (5) further reduced the energy by 3 kcal/mol (Fig. 6B). The

resulting thiolate anion was stabilized by a hydrogen bond with positively charged R451; however, proton transfer from R451 to C432 in (5) along the hydrogen bond yielding (5a) did not further reduce the energy (table S5). Therefore, it is likely that C432 reprotonation proceeds by a different mechanism (see below).

Alternatively to the HAT reaction involving C432, a proton can be transferred from Wat2, which stabilizes the alkyl radical (3). The shift of the negative charge from the flavin to the alkane by bET coupled to proton transfer from Wat2 led to a transient formation of a hydroxyl anion which either interacted with CO₂, forming bicarbonate (6a) directly (Fig. 6, pathway III), or deprotonated R451 (5b) (Fig. 6, pathway II). The presence of CO₂ and water molecules in the active site, in particular Wat1, allows R451 reprotonation concomitant with bicarbonate formation (6), even after the alkane was formed, with a small activation energy (4 kcal/mol; fig. S19). The bicarbonate product derived from Wat1 (6) was 10 kcal/mol lower than the bicarbonate originating from Wat2 (6a), rendering pathway II more energetically favorable than pathway III (Fig. 6B). Energy lowering by bicarbonate formation may also further stabilize product (5) of the HAT reaction (pathway I); in the first step, the thiolate C432 obtains a proton from R451 and/or Wat1 and in the second step, bicarbonate is formed from CO₂ and OH[−] derived from Wat1 (6).

In view of the experimentally observed red-shifted reoxidized flavin intermediate, we compared the flavin excitation energy of the species resulting from the bET reaction and that of the initial dark state (Fig. 6B and table S8). Our computations suggest that the red shift can be explained by formation of various species in which the initial negative charge of the deprotonated carboxylate (1) is either neutralized by formation of CO₂ and deprotonated R451 (5) or shifted away from the flavin by formation of the anionic bicarbonate (6) and (6a) (fig. S20). Additionally, a red-shifted spectrum is caused by hydrogen-bonding interactions of Wat1 with flavin in (5a).

Consistent with the x-ray structures, all active-site models contained the butterfly-bending conformation of the flavin isoalloxazine ring. Flavin bending persisted during geometry optimization of the FAP active-site models (Fig. 6A), in contrast to the essentially

planar optimized geometry of the oxidized and semireduced forms obtained in computations of flavins (36). The significant bending angle in the optimized FAP active-site structures is consistent with the notion that interactions with the protein modulate flavin bending (37). As previously discussed, this bending biases the energy levels of the flavin, favoring flavin reduction (36) and decreasing the excitation energy (table S9), with possible functional implications. In particular, bending diminishes the vertical electron affinity even more than the excited-flavin energy (fig. S21) and thus preferentially reduces the CT-state energy, which should facilitate fET. Thus, flavin bending explains the strongly red-shifted (20-nm) ground-state FAD absorption spectrum of FAP in the dark state compared with free FAD or most flavoproteins, allowing photoexcitation and facile fET up to as far as 530 nm. This is well into the so-called “green gap” (between 500 and 600 nm) in the absorption spectra of chlorophylls that dominate the absorption of algae, thus enhancing the net light-harvesting capacities of FAP.

Role of conserved amino acids in the FAP active site

The active site of CvFAP contains three residues (Y466, C432, and R451) that are strictly conserved and specific to FAPs compared with other GMC oxidoreductases (fig. S23). Y466 and C432 were previously considered as hydrogen atom donor to the alkyl radical R• (followed by bET from FAD^{•−} to the tyrosyl or cysteinyl radical) or, alternatively, proton donor in a proton-coupled back-ET from FAD^{•−} to R• (4, 24). Our quantum chemical calculations additionally suggest R451 as a potential proton donor. To identify the proton donor experimentally, we performed FTIR; in particular, we analyzed possible contributions from deprotonated forms of these three residues in the cryotrapped red-shifted intermediate. Light-induced FTIR difference spectra of CvFAP recorded at 100 K showed only a shift of a ν(S-H) IR mode of cysteine, and no changes in D₂O compared with H₂O that could be assigned to tyrosine vibrations, which does not support deprotonation of either of the two residues under conditions in which the flavin red shift was observed (Fig. 4A, vi, and supplementary text S2). However, a strong negative band was observed at 1606 cm^{−1} in

FTIR difference spectra recorded in D₂O (Fig. 4A, vii). In ¹⁵N-labeled FAP samples, this band downshifted to 1597 cm⁻¹ (Fig. 4A, viii). Both observations support assignment of the band to the guanidium IR mode of an arginine side chain. Absence of a positive counterpart of this band after illumination is indicative of arginine deprotonation in the FAD_{RS} state at 100 K (see supplementary text S2).

To gain further insight into the role of Y466, C432, and R451, we prepared Y466F, C432S, R451A, and R451K mutants and performed activity measurements and extensive structural and spectroscopic characterization (UV-Vis absorption spectra are shown in fig. S24). Mutation of Y466 to phenylalanine affected the catalytic activity only slightly (Fig. 7A), consistent with a previous report (24). The kinetics of both fET to FAD and bET from FAD[•] did not differ much from wild-type (WT) CvFAP (fig. S25C). Furthermore, almost identical FTIR difference spectra were obtained with WT CvFAP and the Y466F mutant (fig.

S26A). Altogether, these results suggest that Y466 does not directly participate in any PT/HAT or ET step in the FAP photocycle, and its role is only briefly discussed in the supplementary text S4.

Mutation of C432 to serine (a much poorer proton and hydrogen atom donor) strongly affected the catalytic activity (Fig. 7A), as reported earlier by Heyes *et al.*, who considered it indicative of HAT from C432 to the alkyl radical R[•] in the WT protein (24). In contrast to these authors, we detected a low but significant catalytic activity (~10% of WT) for the C432S mutant. Because impairment of the catalytic activity by a point mutation may result from structural changes rather than suppression of a direct function of the replaced residue, we examined the C432S mutant protein in more detail. The dark-state crystal structure of C432S was highly similar to WT except for a new water molecule, Wat3, interacting with S432 (2.7 Å) and the O1 oxygen atom of the fatty acid carboxylate (2.5 Å),

which was rotated by ~42° (Fig. 7D). The distance of the carboxylate O2 the flavin N5 increased from 4.0 Å in WT to 5.0 Å.

The time-resolved fluorescence signal of C432S resembled that of WT after the consumption of native substrate(s); however, the fluorescence decay was slightly (~10%) accelerated (Fig. 7B), indicating that the signal reflects mostly intrinsic ¹FAD^{*} decay [mostly because of intersystem crossing (ISC) (4)], with only a small contribution of competing fET to ¹FAD^{*}. The intrinsic fET rate was ~10× slower than ¹FAD^{*} decay in this mutant (see supplementary text S3). Transient absorption signals on the submillisecond time scale were thus dominated by the triplet (fig. S25F), and the formation of FAD_{RS} could not be resolved. There was, however, a small (~15% of WT) long-lived absorption change at 515 nm (where the transient flavin red shift is most prominent in the WT). About two-thirds of it decayed in a few milliseconds, i.e., with similar kinetics as FAD_{RS} in WT [see upper inset of fig.

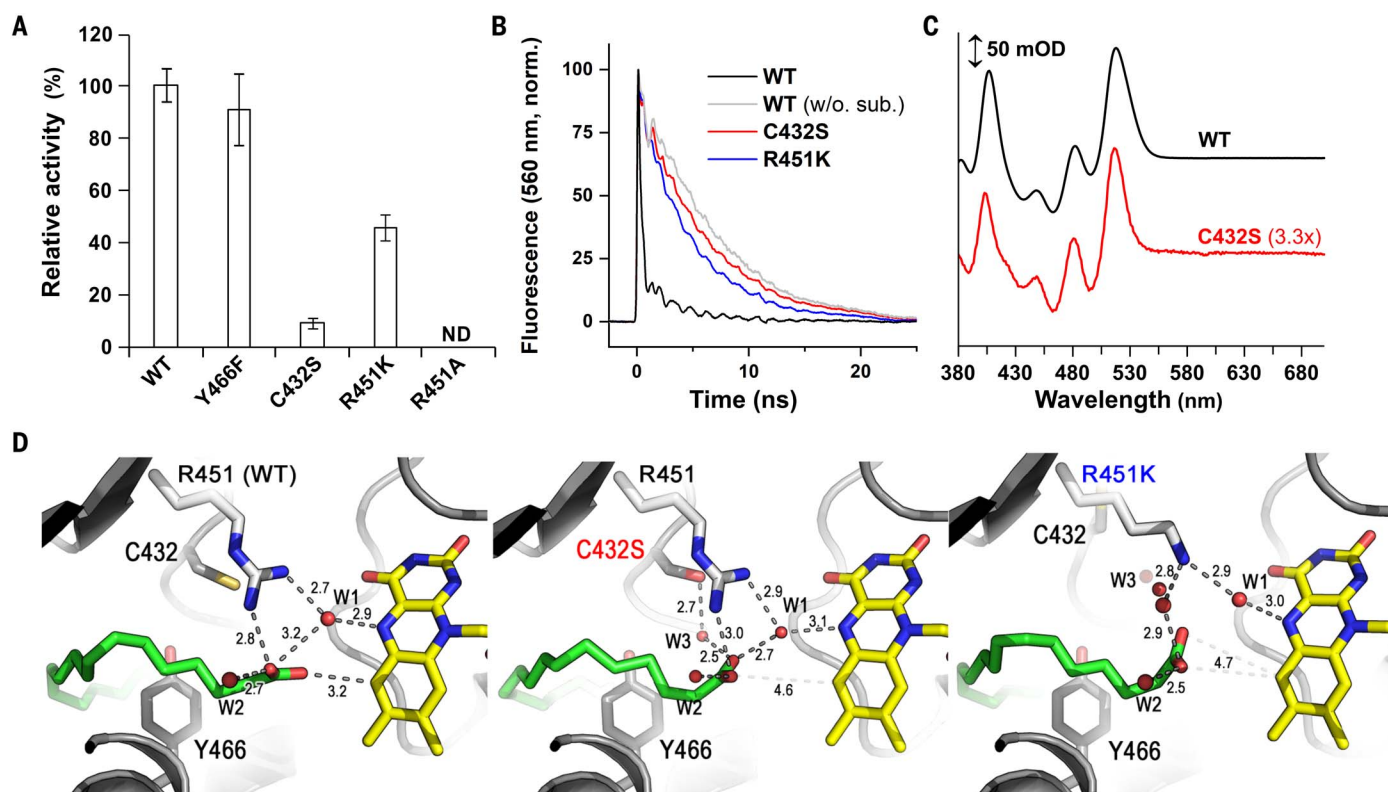
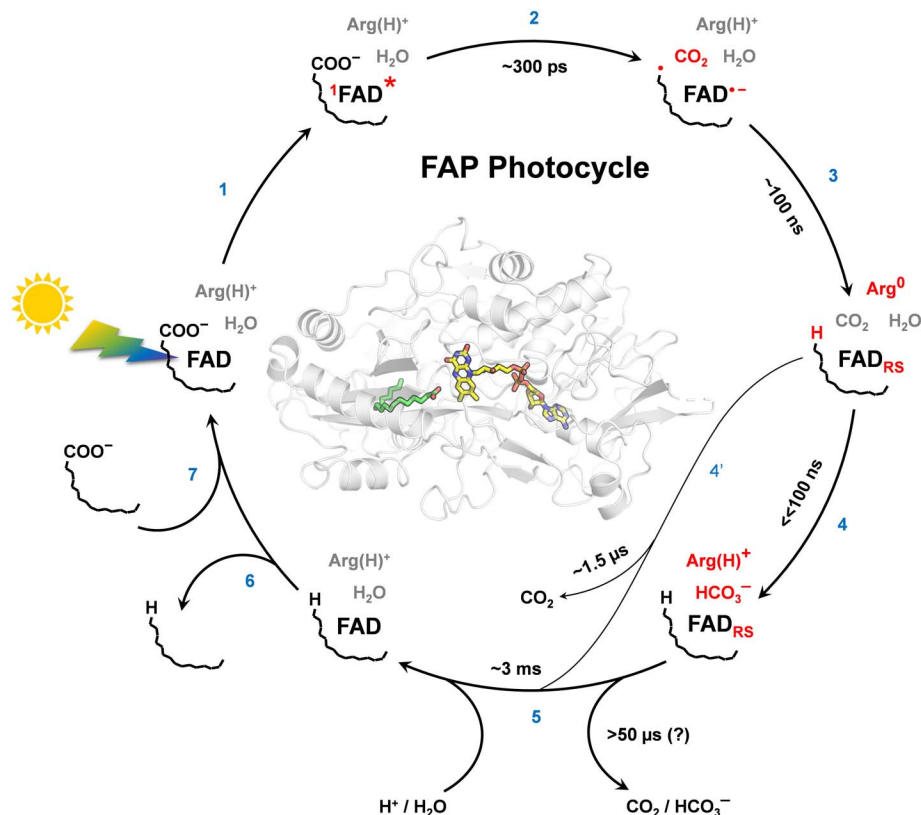


Fig. 7. Impact of mutations of conserved residues on CvFAP activity, ¹FAD^{*} fluorescence decay, spectrum of cryotrapped FAD_{RS}, and active-site structure.

(A) Activities of purified recombinant mutant CvFAPs relative to WT (measured by gas chromatography coupled with mass spectrometry for the Y466F, R451K, and R451A mutants) in the presence of *cis*-vaccenic acid as substrate. Relative activity of the C432S mutant was measured by membrane inlet mass spectrometry to avoid activity underestimation due to low photostability of this particular mutant under continuous illumination conditions. All activities were normalized to FAD content. Mean ± SD is shown (*n* = 5 repeats). ND, not detected. (B) Normalized time-resolved

fluorescence at 560 nm of WT, C432S, and R451K CvFAP in the presence of native substrates (and after their consumption in WT); for Y466F and R451A mutants, see fig. S25B. (C) Light minus dark spectrum of WT and mutant C432S at 200K obtained by cryo-UV-Vis spectroscopy and normalized on FAD content. (D) Structure of the active site of the WT (left), C432S (middle), and R451K (right) mutants. Distances (in angstroms) between substrate (green), FAD (yellow), water molecules (red), and amino acid residues (white or gray) are shown. Compared with WT, in the C432S and R451K mutants, the FA carboxylate is rotated ~50° around an axis defined by the fatty acid atoms O2 and C2.

Fig. 8. Suggested CvFAP photocycle. Upon light excitation (1), fET in ~ 300 ps from the fatty acid anion to $^1\text{FAD}^*$ (observed by ultrafast fluorescence and transient absorption spectroscopies) leads to its quasi-instantaneous decarboxylation (2), as observed by TR-IR and TR-SFX and supported by the computed absence of an energy barrier. bET in ~ 100 ns from $\text{FAD}^{\bullet-}$ (presumably to the alkyl radical) results in formation of red-shifted (re-) oxidized flavin FAD_{RS} ; the H/D KIE suggests that bET is coupled to and/or limited by PT. Cryotrapping FTIR experiments suggest arginine as the final proton donor to the alkyl (3). Concomitantly, most CO_2 ($\sim 75\%$) is transformed (4) to bicarbonate as indicated by TR-IR and cryotrapping FTIR. FAD_{RS} disappears in ~ 3 ms (5) with a H/D KIE > 3 , indicating coupling to PT. Upon alkane release (6), new substrate binds (7). About 25% of the formed CO_2 is not transformed to bicarbonate, likely because it migrates away from the active site within 100 ns, leaving the protein in ~ 1.5 μs (4'). In this minor fraction, arginine (R451) should reprotonate at latest in the ~ 3 ms step (5). Changes after individual steps are marked in red; time constants are for RT.



S25F or figure 3D in [24]). With these indirect indications of FAD_{RS} formation in C432S, we attempted to accumulate this species at a cryogenic temperature. Illumination of the sample at 200 K yielded a spectrum with similar shape (but lower amplitude) as the FAD_{RS} spectrum obtained with WT FAP (Fig. 7C).

When R451 was mutated to alanine, the enzymatic activity was completely abolished (Fig. 7A) and no fET was observed (fig. S25B); in fact, the structure showed that the fatty acid was oriented very differently from that in the WT (see fig. S26D and supplementary text S3 and S4 for details).

When R451 was replaced by lysine (which is also positively charged), the catalytic activity amounted to $\sim 45\%$ of WT (Fig. 7A). The fluorescence decay (Fig. 7B) was distinctly faster (~ 4.5 ns) than in WT without substrate (~ 6.5 ns), consistent with fET occurring for $\sim 30\%$ of the excited flavins. Reoxidation of $\text{FAD}^{\bullet-}$ and formation of FAD_{RS} was clearly resolved and found to be markedly faster (~ 30 ns; fig. S25D) than in WT (~ 100 ns; Fig. 3B, fig. S10A, and supplementary text S3 and S4). The acceleration of the (proton-coupled) bET would be consistent with lysine being a better proton donor than arginine (solution pK_a of Lys is 10.7 versus 12.1 for Arg).

To better understand how R451 affects the active-site architecture, we determined the crystal structure of the R451K mutant in its

dark state at 100 K (Fig. 7D and fig. S26C). The R451K mutant structure differed significantly from WT: Whereas a new water molecule mimicked the NH_2 group of R451 and thereby retained the interaction with the O2 oxygen atom of the fatty acid carboxylate (2.5 Å), the interaction between K451 and the fatty acid O1 oxygen atom induced an $\sim 54^\circ$ rotation of the carboxylate and an increase by 0.6 Å of the distance of the fatty acid O2 to the flavin N5 compared with WT. This created space for a new water molecule, Wat3, akin to the situation in C432S, located between the fatty acid O1 atom (2.4 Å) and K451 (2.8 Å). The close distance of Wat3 and C432 induced a flip of the amino acid stretch T430 to G435, pushing C432 out of the active site and bringing in an additional water molecule. These large structural changes may explain the very different FTIR spectra obtained with the R451K mutant compared with WT (fig. S26B).

Reaction cycle of FAP

Consistent with the strict conservation of C432 and R451 in FAP sequences, even conservative substitutions of these residues resulted in drastic reductions in catalytic activity, in both cases by strongly reducing fET. Unexpectedly, the R451K and C432S mutants shared significant structural modifications with respect to the WT: the presence of a new water molecule, Wat3, close to the fatty acid carboxylate, a rotation of

the carboxylate by $\sim 50^\circ$, a significant elongation of the distance of the fatty acid carboxylate to the flavin N5, as well as small changes in Wat1 location. Quantum chemistry calculations showed that in the C432S mutant, the CT energy increased by 0.2 eV and the electronic coupling reduced fivefold, which is consistent with a much slower observed fET (see supplementary text 6.7 and fig. S22).

These mutants provide important insights into the molecular constraints affording FAP activity: The active site of the WT enzyme is arranged such as to optimize the configuration of the fatty acid carboxylate for fET. Each carboxylate oxygen atom interacts with catalytically important groups (O1: Wat1, O2: R451 and Wat2) while avoiding an inactivating bidentate interaction with R451.

Three possible routes toward alkane formation in FAP were suggested by quantum chemistry (Fig. 6C). Our experimental findings allow assessing the suggested pathways. Pathway I, involving a HAT mechanism to reduce the alkyl radical, as also suggested previously (4, 24), is chemically plausible. However, a number of experimental findings argue against it. First, the C432S mutant retains significant enzymatic activity, suggesting that C432 is not essential for catalysis. Second, in the FAD_{RS} state, only a shift of a thiol S-H vibration is observed by FTIR but no cysteine deprotonation. Third, despite the fact that C432 is

rotated out of the active site in the R451K mutant, this variant is quite active. Although it is possible that C432 rotates back into the active site upon changes in the water structure after CO₂ cleavage, this would not explain the threefold faster bET in R451K. Reaction pathway I (Fig. 6C) seems unlikely, although we cannot rule out that the C432S mutant uses a different mechanism than the WT enzyme. The observation of residual electron density consistent with bicarbonate close to C432 suggests that C432 may stabilize reaction products such as CO₂ and/or bicarbonate away from the original position of the substrate carboxylate.

The other two pathways proceed through PCET (Fig. 6C). Pathway III implies a catalytic role of Wat2 in bicarbonate formation. This mechanism is unlikely, as no changes were observed for Wat2 in the electron density maps derived by TR-SFX. By contrast, 300 ns after photoexcitation, a significant loss of electron density of Wat1 was observed, supporting pathway II. With the cleaved CO₂ present in the active site, as evidenced by cryocrystallography and IR spectroscopy, Wat2 can serve as a proton donor. The transiently deprotonated R451 activates Wat1, resulting in bicarbonate formation in <100 ns. This transformation of CO₂ to bicarbonate is orders of magnitude faster than in solution [tens of seconds (38)], indicating a strong catalytic effect.

R451's role as transient proton donor was a priori unexpected because proton transfers from and to arginine residues are rare (39, 40) due to their relatively high pK_a values. In FAP, the strong basicity of OH⁻ formed from Wat2 by proton-coupled ET to the alkyl radical may allow proton transfer from R451. In addition to this catalytic function, R451 is crucial for the FAP active-site architecture by precisely positioning and orienting the fatty acid head group with respect to FAD and stabilizing the carboxylate in the catalytically active deprotonated form.

Fig. 8 and its legend summarize our comprehensive understanding of the very complex cycle. By combining results obtained by a multitude of experimental techniques and computations, we provide a detailed mechanistic description of the evolution of the reactant (fatty acid) to the products [alka(e)ne and CO₂] and the role of the protein moiety involving a proton-coupled electron-transfer mechanism. We demonstrate partly unexpected structural and dynamic properties of FAP, including features that have not been observed in other flavoproteins and other enzymatic reactions in general. Understanding these catalytic features is an important step in incorporating FAP into the green chemistry toolkit.

Materials and methods summary

The FAP used in all experiments corresponds to residues 76 to 654 of the full-length C₁FAP

(or single mutants thereof obtained by site-directed mutagenesis). WT C₁FAP and C₁FAP mutants expressed in *Escherichia coli* and purified were studied by x-ray crystallography (static and TR-SFX), spectroscopy in solution (FTIR, TR-IR on picosecond to microsecond time scales, time-resolved fluorescence spectroscopy on picosecond to nanosecond time scales, transient absorption spectroscopy on nanosecond to millisecond time scales, and ultrafast visible absorption and fluorescence spectroscopy) and spectroscopy on single crystals (UV-Vis and Raman). Activity assays were based on quantification of hydrocarbons formed (by gas chromatography coupled to mass spectrometry) or CO₂ released (by membrane inlet mass spectrometry). Computational studies involved molecular dynamics simulations and quantum chemistry calculations on C₁FAP and multiple alignments of GMC oxidoreductase protein sequences. Detailed materials and methods are available in the supplementary materials.

REFERENCES AND NOTES

1. L. O. Björn, "Photoactive proteins," in *Photobiology: The Science of Light and Life* (Springer, ed. 3, 2015), pp. 139–150.
2. A. Sancar, Mechanisms of DNA repair by photolyase and excision nuclease (Nobel Lecture). *Angew. Chem. Int. Ed.* **55**, 8502–8527 (2016). doi: [10.1002/anie.201601524](https://doi.org/10.1002/anie.201601524); pmid: [27337655](https://pubmed.ncbi.nlm.nih.gov/27337655/)
3. M. Gabruk, B. Mysliwa-Kurdiel, Light-dependent protochlorophyllide oxidoreductase: phylogeny, regulation, and catalytic properties. *Biochemistry* **54**, 5255–5262 (2015). doi: [10.1021/acs.biochem.5b00704](https://doi.org/10.1021/acs.biochem.5b00704); pmid: [26230427](https://pubmed.ncbi.nlm.nih.gov/26230427/)
4. D. Sorigué et al., An algal photoenzyme converts fatty acids to hydrocarbons. *Science* **357**, 903–907 (2017). doi: [10.1126/science.aan6349](https://doi.org/10.1126/science.aan6349); pmid: [28860382](https://pubmed.ncbi.nlm.nih.gov/28860382/)
5. D. Zhong, Ultrafast catalytic processes in enzymes. *Curr. Opin. Chem. Biol.* **11**, 174–181 (2007). doi: [10.1016/j.cbpa.2007.02.034](https://doi.org/10.1016/j.cbpa.2007.02.034); pmid: [17353141](https://pubmed.ncbi.nlm.nih.gov/17353141/)
6. M. J. Maul et al., Crystal structure and mechanism of a DNA (6-4) photolyase. *Angew. Chem. Int. Ed.* **47**, 10076–10080 (2008). doi: [10.1002/anie.200804268](https://doi.org/10.1002/anie.200804268); pmid: [18956392](https://pubmed.ncbi.nlm.nih.gov/18956392/)
7. P. Müller, J. Yamamoto, R. Martin, S. Iwai, K. Brettel, Discovery and functional analysis of a 4th electron-transferring tryptophan conserved exclusively in animal cryptochromes and (6-4) photolyases. *Chem. Commun. (Camb.)* **51**, 15502–15505 (2015). doi: [10.1039/C5CC06276D](https://doi.org/10.1039/C5CC06276D); pmid: [26355419](https://pubmed.ncbi.nlm.nih.gov/26355419/)
8. A. Mees et al., Crystal structure of a photolyase bound to a CPD-like DNA lesion after in situ repair. *Science* **306**, 1789–1793 (2004). doi: [10.1126/science.1101598](https://doi.org/10.1126/science.1101598); pmid: [15576622](https://pubmed.ncbi.nlm.nih.gov/15576622/)
9. D. J. Heyes, C. N. Hunter, I. H. M. van Stokkum, R. van Grondelle, M. L. Groot, Ultrafast enzymatic reaction dynamics in protochlorophyllide oxidoreductase. *Nat. Struct. Mol. Biol.* **10**, 491–492 (2003). doi: [10.1038/nsb929](https://doi.org/10.1038/nsb929); pmid: [12730687](https://pubmed.ncbi.nlm.nih.gov/12730687/)
10. N. S. Scrutton, M. L. Groot, D. J. Heyes, Excited state dynamics and catalytic mechanism of the light-driven enzyme protochlorophyllide oxidoreductase. *Phys. Chem. Chem. Phys.* **14**, 8818–8824 (2012). doi: [10.1039/c2cp23789j](https://doi.org/10.1039/c2cp23789j); pmid: [22419074](https://pubmed.ncbi.nlm.nih.gov/22419074/)
11. D. J. Heyes et al., Excited-state charge separation in the photochemical mechanism of the light-driven enzyme protochlorophyllide oxidoreductase. *Angew. Chem. Int. Ed.* **54**, 1512–1515 (2015). doi: [10.1002/anie.201409881](https://doi.org/10.1002/anie.201409881); pmid: [25488797](https://pubmed.ncbi.nlm.nih.gov/25488797/)
12. S. Zhang et al., Structural basis for enzymatic photocatalysis in chlorophyll biosynthesis. *Nature* **574**, 722–725 (2019). doi: [10.1038/s41586-019-1685-2](https://doi.org/10.1038/s41586-019-1685-2); pmid: [31645759](https://pubmed.ncbi.nlm.nih.gov/31645759/)
13. C.-S. Dong et al., Crystal structures of cyanobacterial light-dependent protochlorophyllide oxidoreductase. *Proc. Natl. Acad. Sci. U.S.A.* **117**, 8455–8461 (2020). doi: [10.1073/pnas.1920244117](https://doi.org/10.1073/pnas.1920244117); pmid: [32234783](https://pubmed.ncbi.nlm.nih.gov/32234783/)
14. M. A. Emmanuel, N. R. Greenberg, D. G. Oblinsky, T. K. Hyster, Accessing non-natural reactivity by irradiating nicotinamide-dependent enzymes with light. *Nature* **540**, 414–417 (2016). doi: [10.1038/nature20569](https://doi.org/10.1038/nature20569); pmid: [27974767](https://pubmed.ncbi.nlm.nih.gov/27974767/)
15. N. S. Scrutton, Enzymes make light work of hydrocarbon production. *Science* **357**, 872–873 (2017). doi: [10.1126/science.aao4399](https://doi.org/10.1126/science.aao4399); pmid: [28860372](https://pubmed.ncbi.nlm.nih.gov/28860372/)
16. T. Courtney, A. Deiters, Recent advances in the optical control of protein function through genetic code expansion. *Curr. Opin. Chem. Biol.* **46**, 99–107 (2018). doi: [10.1016/j.cbpa.2018.07.011](https://doi.org/10.1016/j.cbpa.2018.07.011); pmid: [30056281](https://pubmed.ncbi.nlm.nih.gov/30056281/)
17. S. Moulin et al., Continuous photoproduction of hydrocarbon drop-in fuel by microbial cell factories. *Sci. Rep.* **9**, 13713 (2019). doi: [10.1038/s41598-019-50261-6](https://doi.org/10.1038/s41598-019-50261-6); pmid: [31548626](https://pubmed.ncbi.nlm.nih.gov/31548626/)
18. W. Zhang et al., Hydrocarbon synthesis via photoenzymatic decarboxylation of carboxylic acids. *J. Am. Chem. Soc.* **141**, 3116–3120 (2019). doi: [10.1021/jacs.8b12282](https://doi.org/10.1021/jacs.8b12282); pmid: [30673222](https://pubmed.ncbi.nlm.nih.gov/30673222/)
19. M. Am et al., Low carbon strategies for sustainable bio-alkane gas production and renewable energy. *Energy Environ. Sci.* (2020).
20. N. A. Herman, W. Zhang, Enzymes for fatty acid-based hydrocarbon biosynthesis. *Curr. Opin. Chem. Biol.* **35**, 22–28 (2016). doi: [10.1016/j.cbpa.2016.08.009](https://doi.org/10.1016/j.cbpa.2016.08.009); pmid: [27573483](https://pubmed.ncbi.nlm.nih.gov/27573483/)
21. J. Xu et al., Light-driven kinetic resolution of α -functionalized carboxylic acids enabled by an engineered fatty acid photodecarboxylase. *Angew. Chem. Int. Ed.* **58**, 8474–8478 (2019). doi: [10.1002/anie.201903165](https://doi.org/10.1002/anie.201903165); pmid: [31033108](https://pubmed.ncbi.nlm.nih.gov/31033108/)
22. D. Sorigué et al., Microalgae synthesize hydrocarbons from long-chain fatty acids via a light-dependent pathway. *Plant Physiol.* **171**, 2393–2405 (2016). doi: [10.1104/pp.16.00462](https://doi.org/10.1104/pp.16.00462); pmid: [27288359](https://pubmed.ncbi.nlm.nih.gov/27288359/)
23. S. Moulin, A. Beyly, S. Blangy, B. Légeret, M. Floriani, A. Burlacot, D. Sorigué, Y. Li-Beisson, G. Peltier, F. Beisson, Fatty acid photodecarboxylase is an ancient photoenzyme responsible for hydrocarbon formation in the thylakoid membranes of algae. *bioRxiv* 166330 [Preprint]. 23 June 2020. <https://doi.org/10.1101/2020.06.23.166330>
24. D. J. Heyes et al., Photochemical mechanism of light-driven fatty acid photodecarboxylase. *ACS Catal.* **10**, 6691–6696 (2020). doi: [10.1021/acscatal.0c01684](https://doi.org/10.1021/acscatal.0c01684); pmid: [32905273](https://pubmed.ncbi.nlm.nih.gov/32905273/)
25. T. Senda, M. Senda, S. Kimura, T. Ishida, Redox control of protein conformation in flavoproteins. *Antioxid. Redox Signal.* **11**, 1741–1766 (2009). doi: [10.1089/ars.2008.2348](https://doi.org/10.1089/ars.2008.2348); pmid: [19243237](https://pubmed.ncbi.nlm.nih.gov/19243237/)
26. A. K. Rohr, H.-P. Hersleth, K. K. Andersson, Tracking flavin conformations in protein crystal structures with Raman spectroscopy and QM/MM calculations. *Angew. Chem. Int. Ed.* **49**, 2324–2327 (2010). doi: [10.1002/anie.200907143](https://doi.org/10.1002/anie.200907143); pmid: [20187055](https://pubmed.ncbi.nlm.nih.gov/20187055/)
27. A. Aleksandrov, A molecular mechanics model for flavins. *J. Comput. Chem.* **40**, 2834–2842 (2019). doi: [10.1002/jcc.26061](https://doi.org/10.1002/jcc.26061); pmid: [31471978](https://pubmed.ncbi.nlm.nih.gov/31471978/)
28. H. N. Chapman et al., Femtosecond X-ray protein nanocrystallography. *Nature* **470**, 73–77 (2011). doi: [10.1038/nature09750](https://doi.org/10.1038/nature09750); pmid: [21293373](https://pubmed.ncbi.nlm.nih.gov/21293373/)
29. K. Hirata et al., Determination of damage-free crystal structure of an X-ray-sensitive protein using an XFEL. *Nat. Methods* **11**, 734–736 (2014). doi: [10.1038/nmeth.2962](https://doi.org/10.1038/nmeth.2962); pmid: [24813624](https://pubmed.ncbi.nlm.nih.gov/24813624/)
30. S. P. Laptinok et al., Ultrafast real-time visualization of active site flexibility of flavoenzyme thymidylate synthase ThyX. *Proc. Natl. Acad. Sci. U.S.A.* **110**, 8924–8929 (2013). doi: [10.1073/pnas.1218729110](https://doi.org/10.1073/pnas.1218729110); pmid: [23671075](https://pubmed.ncbi.nlm.nih.gov/23671075/)
31. L. H. Jones, E. McLaren, Infrared Absorption Spectra of SO₂ and CO₂ in Aqueous Solution. *J. Chem. Phys.* **28**, 995 (1958). doi: [10.1063/1.1744329](https://doi.org/10.1063/1.1744329)
32. L. Antonucci, A. Bonvalet, X. Solinas, L. Daniault, M. Joffre, Arbitrary-detuning asynchronous optical sampling with amplified laser systems. *Opt. Express* **23**, 27931–27940 (2015). doi: [10.1364/OE.23.027931](https://doi.org/10.1364/OE.23.027931); pmid: [26480451](https://pubmed.ncbi.nlm.nih.gov/26480451/)
33. X. Solinas, L. Antonucci, A. Bonvalet, M. Joffre, Multiscale control and rapid scanning of time delays ranging from picosecond to millisecond. *Opt. Express* **25**, 17811–17819 (2017). doi: [10.1364/OE.25.017811](https://doi.org/10.1364/OE.25.017811); pmid: [28789272](https://pubmed.ncbi.nlm.nih.gov/28789272/)
34. B. A. Diner, D. A. Force, D. W. Randall, R. D. Britt, Hydrogen bonding, solvent exchange, and coupled proton and electron transfer in the oxidation and reduction of redox-active tyrosine Y(2) in Mn-depleted core complexes of photosystem II. *Biochemistry* **37**, 17931–17943 (1998). doi: [10.1021/bi981894r](https://doi.org/10.1021/bi981894r); pmid: [9922161](https://pubmed.ncbi.nlm.nih.gov/9922161/)
35. J.-P. Colletier, G. Schirò, M. Weik, "Time-resolved serial femtosecond crystallography, towards molecular movies of

- biomolecules in action," in *X-Ray Free Electron Lasers: A Revolution in Structural Biology*, S. Boutet, P. Fromme, M. S. Hunter, Eds. (Springer, 2018), pp. 331–356.
36. J. D. Walsh, A.-F. Miller, Flavin reduction potential tuning by substitution and bending. *J. Mol. Struct. THEOCHEM* **623**, 185–195 (2003). doi: [10.1016/S0166-1280\(02\)00719-4](https://doi.org/10.1016/S0166-1280(02)00719-4)
 37. B. W. Lennon, C. H. Williams Jr., M. L. Ludwig, Crystal structure of reduced thioredoxin reductase from *Escherichia coli*: Structural flexibility in the isoalloxazine ring of the flavin adenine dinucleotide cofactor. *Protein Sci.* **8**, 2366–2379 (1999). doi: [10.1110/ps.8.11.2366](https://doi.org/10.1110/ps.8.11.2366); pmid: [10595539](https://pubmed.ncbi.nlm.nih.gov/10595539/)
 38. N. McCann et al., Kinetics and mechanism of carbamate formation from CO₂(aq), carbonate species, and monoethanolamine in aqueous solution. *J. Phys. Chem. A* **113**, 5022–5029 (2009). doi: [10.1021/jp810564z](https://doi.org/10.1021/jp810564z); pmid: [19338322](https://pubmed.ncbi.nlm.nih.gov/19338322/)
 39. Y. Xiao, M. S. Hutson, M. Belenky, J. Herzfeld, M. S. Braiman, Role of arginine-82 in fast proton release during the bacteriorhodopsin photocycle: A time-resolved FT-IR study of purple membranes containing ¹⁵N-labeled arginine. *Biochemistry* **43**, 12809–12818 (2004). doi: [10.1021/bi049238g](https://doi.org/10.1021/bi049238g); pmid: [15461453](https://pubmed.ncbi.nlm.nih.gov/15461453/)
 40. P. J. Silva, C. Schulz, D. Jahn, M. Jahn, M. J. Ramos, A tale of two acids: When arginine is a more appropriate acid than H₃O⁺. *J. Phys. Chem. B* **114**, 8994–9001 (2010). doi: [10.1021/jp100961s](https://doi.org/10.1021/jp100961s); pmid: [20553007](https://pubmed.ncbi.nlm.nih.gov/20553007/)

ACKNOWLEDGMENTS

We thank J. Woodhouse for help with microcrystallization, L. Uriarte for help with spectroscopy experiments on crystals, G. Nass Kovacs for preparation of injection conditions, M. Tarnawski for FAP stability measurements, F. Maia for helpful discussions and uploading the SFX data to CXIDB.org, M. Philibert and the GRAP platform for custom manufacturing of scientific equipment. The ESRF is acknowledged for access to beamlines via its in-house research program. This work used the iCOS Laboratory, which is a platform of the Grenoble Instruct-ERIC Centre (ISBG; UMS 3518 CNRS-CEA-UJF-EMBL) within the Grenoble Partnership for Structural Biology (PSB). The IBS acknowledges integration into the Interdisciplinary Research Institute of Grenoble (IRIG, CEA) and financial support by the CEA, the CNRS, and the UGA. The present work has benefited from the platform of Biophysics of I2BC supported by French

Infrastructure for Integrated Structural Biology (FRISBI) ANR-10-INBS-05 and from the platform Heliobiotec (BIAM). The experiments were performed at the Linac Coherent Light Source (LCLS), SLAC National Accelerator Laboratory. Use of the LCLS is supported by the U.S. Department of Energy, Office of Science, Office of Basic Energy Sciences under Contract no. DE-AC02-76SF00515. Part of the sample injector used at LCLS for this research was funded by the National Institutes of Health, P41GM103393, formerly P41RR001209. **Funding:** This work was supported by ANR SNAPsHOTs to F.B., M.W., P.M., K.B., M.H.V., P.A., R.H., and C.B.; ANR Photoalkane to G.P.; ANR SignalBioRNJ to Y.L.-B.; ANR BioXFEL to M.W.; ERC Consolidator Grant STepLADDER (724362) to T.R.M.B.; a Chinese Scholarship Council fellowship to B.Z.; and a MENESR–Univ. Grenoble Alpes fellowship to K.H.; a grant from the Chevreul Institute and the Ministère de l'Enseignement Supérieur et de la Recherche and the Région Nord-Pas de Calais (FEDER) to M.S. **Author contributions:** F.B., M.W., P.A., P.M., I.S., K.B., M.H.V., C.B., and T.D. designed and organized the project. J.-P.C., M.J., T.R.M.B., and A.R. supervised parts of the project. D.S., S. Blangy, P.S., S. Cuiné, B.L., S.M., Y.L.-B., G.P., E.H., and F.B. analyzed FAP sequences, generated mutants, expressed and purified the FAPs, and performed activity assays. D.S., S. Blangy, E.H., and P.A. produced crystals for synchrotron experiments. P.A., G.G., A.R., D.N., P.L., I.S., and D.S. acquired synchrotron diffraction data. G.G., P.A., and A.R. performed *in crystallo* optical spectroscopies, and P.A., I.S., G.G., P.L., and A.R. interpreted these data. D.S., R.H., and C.B. built the setup for cryogenic light-induced FTIR difference spectroscopy and acquired and analyzed the data. A. Bonvalet, A. Benachir, and D.S. optimized and performed multiscale TR-IR experiments. L.A., X.S., A. Bonvalet, and M.J. conceived and developed multiscale TR-IR spectroscopy and adapted for FAP experiments. A. Bonvalet., L.A., M.J., and M.H.V. analyzed TR-IR data. M.H.V. performed and analyzed femtosecond pump-probe absorption and fluorescence spectroscopy. B.Z. and M.H.V. performed and analyzed picosecond-pump power dependence spectroscopy. A.A. performed molecular dynamics simulations. D.S., S. Blangy, and K.H. produced microcrystals for SFX experiments, and K.H., J.-P.C., and M.W. tested their diffraction quality at the ESRF. M.S., K.H., and D.S. performed time-resolved emission and absorption spectroscopy on microcrystals. T.R.M.B., M.C., S. Boutet, J.-P.C., N.C., R.B.D.,

L.F., A.G., M.L.G., K.H., M.H., M.K., T.J.L., G.S., I.S., R.L.S., and M.W. performed SFX experiments. R.L.S., R.B.D., M.L.G., and M.K. performed sample injection. S. Carbajo, G.S. and M.C. carried out laser work at the LCLS. S. Boutet and T.J.L. prepared and performed SFX data collection. L.F., M.H., N.C., J.-P.C., and T.R.M.B. performed online SFX data analysis. K.H., N.C., J.-P.C., A.G., and T.R.M.B. performed offline SFX data processing. K.H., J.-P.C., N.C., M.W., T.R.M.B., and I.S. analyzed SFX data. M.B., K.B., and P.M. built the setups for picosecond-nanosecond time-resolved fluorescence and nanosecond-millisecond transient absorption spectroscopy. D.S., P.S., B.Z., P.M., and K.B. performed the measurements. P.M. and K.B. analyzed the data. T.D. performed quantum chemistry calculations and provided mechanistic insight. F.B., P.M., K.B., M.H.V., I.S., P.A., T.D., M.W., C.B., and D.S. wrote the paper. All authors discussed the results. **Competing interests:** L.A., X.S., A. Bonvalet, and M.J. are authors of a patent describing the general principle of ADASOPS (FR1155799, US10190972B2). The authors declare no other competing interests. **Data and materials availability:** All data are available in the manuscript, the supplementary materials, or at publicly accessible repositories. Atomic coordinates of protein structures have been deposited in the Protein Data Bank under accession nos. 6YRU, 6YRV, 6YRX, 6YRZ, 6YS1, 6YS2, 6ZH7, and 7AV4. SFX diffraction images of FAP microcrystals have been deposited in the Coherent X-ray Imaging Data Bank website (CXIDB) with accession ID 177 (<https://cxidb.org/id-177.html>).

SUPPLEMENTARY MATERIALS

science.sciencemag.org/content/372/6538/eabd5687/suppl/DC1

Materials and Methods

Supplementary Text S1 to S6

Figs. S1 to S31

Tables S1 to S11

References (41–121)

MDAR Reproducibility Checklist

[View/request a protocol for this paper from Bio-protocol.](#)

29 June 2020; accepted 17 February 2021
10.1126/science.abd5687